

A four-dimensional asynchronous ensemble square-root filter (4DEnSRF) algorithm and tests with simulated radar data

Shizhang Wang,^{a,b} Ming Xue^{b,c*} and Jinzhong Min^a

^aNanjing University of Information Science and Technology, Nanjing, China

^bCenter for Analysis and Prediction of Storms, University of Oklahoma, Norman, OK, USA

^cSchool of Meteorology, University of Oklahoma, Norman, OK, USA

*Correspondence to: M. Xue, Center for Analysis and Prediction of Storms, University of Oklahoma, 120 David L. Boren Blvd, Norman, OK 73072, USA. E-mail: mxue@ou.edu

A four-dimensional ensemble square-root filter algorithm (4DEnSRF) is designed to assimilate high-frequency asynchronous observations distributed over time. Given the serial nature of the EnSRF, the 4DEnSRF algorithm pre-calculates observation priors from ensemble model states at observation times and updates the observation priors at asynchronous observational times using the filter. These updated observation posteriors are used to update model state variables at the analysis time. Such an algorithm is able to utilize more observations collected over time with fewer analysis cycles, thereby reducing computational costs and potentially improving filter performance. The 4DEnSRF algorithm is tested using simulated Doppler radar data for a convective storm. The radar data are simulated elevation-by-elevation, grouped into batches with different time intervals and then assimilated with analysis cycles of the same lengths. Parallel sets of experiments using 4DEnSRF and the regular EnSRF are performed for comparison, with varying data batch or cycle lengths of 1 to 20 min. For longer time intervals, EnSRF either assumes that all data collected within the time window are valid at the same analysis time, or uses only elevations collected within a shorter time interval centered at the analysis time. Results show that 4DEnSRF outperforms EnSRF when the cycle length is more than 1 min. Observation timing error is the main cause of the performance degradation with EnSRF for both analysis and forecast; the longer the cycle length, the worse the degradation. For long cycle lengths, 4DEnSRF improves the analysis by utilizing more data whereas the EnSRF performs well only when data far away from the analysis time are discarded. Assimilating only a couple of scan elevations at a time using EnSRF with very short cycles can introduce imbalances into the model state that degrades the subsequent analyses and forecasts. Copyright © 2012 Royal Meteorological Society

Key Words: Ensemble Kalman Filter; OSSE; radar data assimilation

Received 9 March 2012; Revised 8 May 2012; Accepted 15 May 2012; Published online in Wiley Online Library 26 June 2012

Citation: Wang S, Xue M, Min J. 2013. A four-dimensional asynchronous ensemble square-root filter (4DEnSRF) algorithm and tests with simulated radar data. *Q. J. R. Meteorol. Soc.* **139**: 805–819. DOI:10.1002/qj.1987

1. Introduction

Frequent observations from modern remote sensing platforms such as weather radar can provide nearly continuous

observations of weather systems. Effective utilization of such frequent observations and maximum extraction of their information content for model initialization pose a great challenge. A common practice for sequential data

assimilation (DA) algorithms such as the three-dimensional variational (3DVAR) technique and ensemble Kalman filter (EnKF; Evensen, 1994) is to group frequent observations into small batches and perform the analyses at frequent intervals through so-called intermittent assimilation cycles (e.g. Hu and Xue, 2007; Dowell and Wicker, 2009). This approach involves frequent stopping and restarting of the prediction model, which can introduce shock to the prediction system every time a new analysis is performed. In the case of EnKF, the writing and reading of a full ensemble of states at least twice each cycle carry very high data input/output (I/O) costs.

Assimilating radar data at volume-scan or subvolume-scan intervals can be computationally very expensive given the high frequency of the data. Using longer assimilation cycles can save computational costs, where observations taken over a chosen time window are often all assumed to be valid at the analysis time. This approach is common in assimilating frequent radar data. It can, however, introduce large timing error when the weather system is fast evolving, as in the case of a fast moving convective storm. Another way to reduce the computational cost is to discard some observations not close enough to the analysis time (e.g. Hu and Xue, 2007; Zhang *et al.*, 2009). The obvious drawback is that some valuable observations are not used.

A better approach to more fully utilize observations collected over time is to employ four-dimensional assimilation algorithms. In contrast to three-dimensional algorithms, four-dimensional algorithms use observations distributed over time simultaneously and at the times when they are collected. Sakov *et al.* (2010; S10 hereafter) proposed a generic asynchronous ensemble Kalman filter (AEnKF) that allows for the assimilation of asynchronous observations before, at and after the analysis time. The algorithm has a close relationship with the ensemble Kalman smoother (EnKS) (Evensen and van Leeuwen, 2000). The four-dimensional local ensemble Kalman filter (4D-LEnKF) of Hunt *et al.* (2004) and the four-dimensional local ensemble transform Kalman filter (4D-LETKF) of Hunt *et al.* (2007) can be considered specific implementations of the AEnKF algorithm. As pointed out by S10, in the case of a perfect, linear model, the analysis ensemble mean and ensemble perturbations in EnKF can be written as the linear combination or linear transform of the forecast ensemble perturbations. This transform matrix, calculated from the background forecast ensembles at the observation times, can be used for the assimilation of observations at other times as long as the evolution of ensemble perturbations is linear (Evensen, 2003). When the transform matrix is used for the assimilation of observations at other times, the Kalman gain in the EnKF formula contains covariances involving ensemble priors at different times; they are therefore referred to as asynchronous covariances. Through the asynchronous covariances between background states at the observation times and the analysis time, AEnKF can directly use asynchronous observations to update the model state at the analysis time. In addition, AEnKF can be implemented for different EnKF variants in principle (S10).

Hunt *et al.* (2004) showed that for the Lorenz-96 (Lorenz, 1996) model, the performance of their 4D-LEnKF is considerably better than that of the standard EnKF and EnKF using time-interpolated data. In Hunt *et al.* (2007), 4D-LETKF is compared with the National Centers for Environmental Prediction (NCEP) spectral statistical interpolation (SSI)

3DVAR system using a T62 model in a perfect model scenario; they also found 4D-LETKF-based forecasts to be more accurate than those from the SSI analyses. These studies show positive impacts using four-dimensional algorithms even when the linear model assumption is not strictly valid. More recently, Compo *et al.* (2011) applied the ensemble square root filter (EnSRF; Whitaker and Hamill, 2002; hereafter WH02) to a global reanalysis project that assimilated surface pressure observations only, and mentioned in passing the use of hourly observations not taken at the 6 h analysis times through an extension of the EnSRF algorithm. Their implementation did not seem to apply time localization.

For a storm-scale radar DA problem, the model dynamics and physics are more highly nonlinear. Additionally, some observation operators are also nonlinear. The performance of an AEnKF algorithm in storm-scale applications has yet to be examined. It would be interesting to see how well an asynchronous extension of the serial EnSRF (Whitaker and Hamill, 2002) would work, given that radar DA studies have almost exclusively used the EnSRF algorithm or algorithms that are very similar (e.g. Snyder and Zhang, 2003; Zhang *et al.*, 2004; Tong and Xue, 2005; Xue *et al.*, 2006; Snook *et al.*, 2011).

In this article we develop an AEnKF implementation of EnSRF, which we refer to as the 4D-EnSRF. As the first step to evaluate the algorithm, we employ observing system simulation experiments (OSSEs) that use simulated radar data. With OSSEs the truth is known, allowing us to unambiguously assess the performance of the algorithms. The OSSE framework also allows us to simulate radar data in different configurations and to perform experiments that are not easy to do with real data. We compare the 4D-EnSRF with the regular EnSRF. The rest of this article is organized as follows. In section 2 we review the general EnSRF algorithm and then describe our 4D-EnSRF algorithm and its implementation. Model settings, radar observation simulation and OSSE configurations are described in section 3. The OSSE results are discussed in section 4 and a summary and conclusions are given in section 5.

2. Formulation and implementation of 4D-EnSRF

2.1. The regular EnSRF algorithm

According to S10, the linear ensemble update in EnKF can be written in a generic form as

$$\bar{\mathbf{x}}^a = \bar{\mathbf{x}}^b + \mathbf{X}'^b \mathbf{G} \mathbf{s}, \quad (1)$$

$$\mathbf{X}'^a = \mathbf{X}'^b + \mathbf{X}'^b \mathbf{T}, \quad (2)$$

where \mathbf{x} is the state vector, overbar is for ensemble mean, superscript a and b denote the analysis and the analysis background and prime denotes ensemble perturbation. $\mathbf{X}'^b = [\mathbf{x}'_1, \mathbf{x}'_2, \dots, \mathbf{x}'_m]$ is the perturbation forecast ensemble with an ensemble size of m and

$$\mathbf{s} = \mathbf{R}^{-1/2} (\mathbf{y}^o - \mathbf{H} \bar{\mathbf{x}}^b) / \sqrt{m-1} \quad (3)$$

is the scaled innovation vector; with \mathbf{y}^o the observation vector, \mathbf{R} the observation covariance matrix and \mathbf{H} the linearized observation operator. In S10, matrices \mathbf{G} and \mathbf{T} in Eqs (1) and (2) are represented in terms of scaled observation ensemble priors, \mathbf{S} ,

$$\mathbf{S} = \mathbf{R}^{-1/2} \mathbf{H} \mathbf{X}'^b / \sqrt{m-1}. \quad (4)$$

Therefore, \mathbf{G} is written as

$$\mathbf{G} = \mathbf{S}^T(\mathbf{I} + \mathbf{S}\mathbf{S}^T)^{-1}, \quad (5)$$

where \mathbf{I} is an identity matrix. Matrix \mathbf{G} is not dependent on the specific ensemble analysis algorithm used, but transform matrix \mathbf{T} is. For the EnSRF algorithm of WH02, \mathbf{T} has the following form:

$$\mathbf{T} = -\alpha\mathbf{G}\mathbf{S} \quad (6)$$

where α is a factor introduced by WH02 in the deterministic EnSRF algorithm and is given by

$$\alpha = [1 + \sqrt{\mathbf{R}(\mathbf{H}\mathbf{P}^b\mathbf{H}^T + \mathbf{R})^{-1}}]^{-1}, \quad (7)$$

where

$$\mathbf{P}^b = \mathbf{X}'^b(\mathbf{X}''^b)^T. \quad (8)$$

As mentioned in WH02, α is only valid for single observation analysis, so is the \mathbf{T} in the form of Eq. (6).

Substituting Eq. (6) into Eqs (1) and (2) gives the EnSRF formula; however, these equations are not in the form presented by WH02 and commonly used in storm-scale DA, including the advanced regional prediction system (ARPS) EnKF framework used in this study (Xue *et al.*, 2006). Here we will show that they are equivalent.

Substituting Eq. (4) into Eq. (5), we can rewrite matrix \mathbf{G} as

$$\mathbf{G} = \sqrt{m-1}(\mathbf{H}\mathbf{X}'^b)^T\mathbf{R}^{-1/2}(\mathbf{I} + \mathbf{R}^{-1/2}\mathbf{H}\mathbf{X}'^b\mathbf{X}''^b\mathbf{H}^T\mathbf{R}^{-1/2})^{-1} \quad (9a)$$

$$= \sqrt{m-1}(\mathbf{H}\mathbf{X}'^b)^T(\mathbf{R} + \mathbf{H}\mathbf{P}^b\mathbf{H}^T)^{-1}\mathbf{R}^{1/2}. \quad (9b)$$

Using Eqs (3) and (9b), the correction to the ensemble mean, $\mathbf{X}'^b\mathbf{G}\mathbf{s}$, in Eq. (1) can be expressed as

$$\mathbf{X}'^b\mathbf{G}\mathbf{s} = \mathbf{X}'^b[(\mathbf{H}\mathbf{X}'^b)^T(\mathbf{R} + \mathbf{H}\mathbf{P}^b\mathbf{H}^T)^{-1}(\mathbf{y} - \mathbf{H}\bar{\mathbf{x}}^b)] \quad (10a)$$

$$= \mathbf{K}(\mathbf{y}^o - \mathbf{H}\bar{\mathbf{x}}^b), \quad (10b)$$

where \mathbf{K} is the typical Kalman gain

$$\mathbf{K} = \mathbf{P}^b\mathbf{H}^T(\mathbf{H}\mathbf{P}^b\mathbf{H}^T + \mathbf{R})^{-1}, \quad (11)$$

using Eq. (8). Similarly, the $\mathbf{X}'^b\mathbf{T}$ in Eq. (2) can also be rewritten using Eqs (4), (5) and (6)

$$\mathbf{X}'^b\mathbf{T} = -\alpha\mathbf{X}'^b[(\mathbf{H}\mathbf{X}'^b)^T(\mathbf{R} + \mathbf{H}\mathbf{P}^b\mathbf{H}^T)^{-1}\mathbf{H}\mathbf{X}'^b] \quad (12a)$$

$$= -\alpha\mathbf{K}\mathbf{H}\mathbf{X}'^b. \quad (12b)$$

Plugging Eqs (10b) and (12b) into Eqs (1) and (2) gives the commonly used EnSRF formula. Therefore, the key difference between the WH02 formulation (and the original EnKF formulation as presented by Evensen, 1994), and the S10 formulation (as well as the LETKF formulation: Hunt *et al.*, 2007; Yang *et al.*, 2009) is the treatment of ensemble perturbation matrix \mathbf{X}'^b in the equations. In the former, \mathbf{X}'^b is absorbed into the Kalman gain matrix \mathbf{K} and used to calculate the background error covariance, whereas in the latter, \mathbf{X}'^b is kept explicitly in the update equations with 'weight' matrices applied to it to give the analysis increments.

2.2. The 4DEnSRF algorithm

The second terms on the right-hand side of Eqs (1) and (2) are the corrections to the ensemble mean and ensemble perturbations, respectively, written as $\delta\bar{\mathbf{x}}$ and $\delta\mathbf{X}'$. Sakov *et al.* (2010) pointed out that the evolution of these corrections from t_0 to t_1 can be approximated by, respectively,

$$\delta\bar{\mathbf{x}}_1 \sim \mathbf{M}_{01}\delta\bar{\mathbf{x}}_0 = \mathbf{M}_{01}\mathbf{X}'_0^b\mathbf{G}_0\mathbf{s}_0 \sim \mathbf{X}'_1^b\mathbf{G}_0\mathbf{s}_0, \quad (13)$$

$$\delta\mathbf{X}'_1 \sim \mathbf{M}_{01}\delta\mathbf{X}'_0 = \mathbf{M}_{01}\mathbf{X}'_0^b\mathbf{T}_0 \sim \mathbf{X}'_1^b\mathbf{T}_0, \quad (14)$$

where \mathbf{M}_{01} is the tangent linear propagator for the forecast trajectory from time t_0 to t_1 , subscripts 0 and 1 are used to tag variables at t_0 and t_1 , respectively, and the ' \sim ' denotes 'asymptotically equal'. Substituting approximations in Eqs (13) and (14) into Eqs (1) and (2), respectively, gives the AEnKF update equations

$$\bar{\mathbf{x}}_1^a = \bar{\mathbf{x}}_1^b + \mathbf{X}'_1^b\mathbf{G}_0\mathbf{s}_0, \quad (15)$$

$$\mathbf{X}'_1^a = \mathbf{X}'_1^b + \mathbf{X}'_1^b\mathbf{T}_0, \quad (16)$$

which use matrices \mathbf{G}_0 and \mathbf{T}_0 calculated from observation priors $\mathbf{H}\mathbf{X}'^b$ at time t_0 , and observation innovations given by \mathbf{s}_0 to update ensemble states at time t_1 .

As shown earlier, Eqs (15) and (16) can be rewritten into the EnSRF form based on Eqs (10b) and (12b) as follows:

$$\bar{\mathbf{x}}_1^a = \bar{\mathbf{x}}_1^b + \mathbf{K}_{01}(\mathbf{y}^o - \mathbf{H}\bar{\mathbf{x}}_0^b), \quad (17)$$

$$\mathbf{X}'_1^a = \mathbf{X}'_1^b - \alpha_0\mathbf{K}_{01}\mathbf{H}\mathbf{X}'_0^b, \quad (18)$$

where

$$\mathbf{K}_{01} = \mathbf{X}'_1^b(\mathbf{H}\mathbf{X}'_0^b)^T(\mathbf{R}_0 + \mathbf{H}\mathbf{P}_0^b\mathbf{H}^T)^{-1} \quad (19)$$

is the Kalman gain for updating model state at t_1 using observations collected at t_0 and α_0 is factor α in Eq. (7) calculated using priors at t_0 . In Eq. (19), $\mathbf{X}'_1^b(\mathbf{H}\mathbf{X}'_0^b)^T$ represents the asynchronous covariance between the model states at the analysis time and the observation priors at the observation times. Comparing Eqs (10b), (11) and (12b) with Eqs (17), (18) and (19), the only difference is that the observation prior at the *analysis* time is replaced by the observation prior calculated at the *observation* time. For the EnSRF algorithm, Eqs (17) and (18) are applied to each observation distributed over time serially (one at a time). Therefore, it is sufficient to know the observation priors at the observation times for the 4DEnSRF analysis; the full model states at observation times are not required. This is important because otherwise the full model states at the observation times would have to be updated by each of the observations, which would be computationally expensive.

Equations (13) and (14) are based on the tangent linear approximation to the forecast system. However, as pointed out in S10, as long as the impact of the nonlinear part of forecast system is not very significant, Eqs (17) and (18) may still be valid. Being based on forward-integrating tangent linear equations, Eqs (13) and (14) provide only a derivation of the asynchronous filter for updating the model state using past data. However, as pointed out by S10, the asynchronous filter can be used to assimilate future data also. In that case, the formulation is equivalent to an

ensemble Kalman smoother (e.g. Evensen and van Leeuwen, 2000); in fact, Evensen (2003) presented the equations (their Eqs (103) and (104)) for updating the current state using future observations as a smoother, and the formulation is the same as the filter (see their Eqs (54) and (72)) except for the differences in relative state and observation times. Therefore, AEnKF also can be used to update a model state at a time prior to the observation times. Therefore, belonging to the family of AEnKF, 4DEnSRF has the ability to assimilate past and current data as a filter and future data as a smoother. Algorithmically, the latter involves calculating covariance between the model state at the analysis time and observation priors at a future time.

2.3. The implementation of asynchronous 4DEnSRF

According to Eqs (17) and (18), 4DEnSRF requires the precalculation of observation priors before performing the analysis. This precalculation can be done within the forecast model during the advancement of each member to save on data I/O cost. We have actually implemented this capability within the ARPS model (Xue *et al.*, 2003) and its EnKF DA system. For this current study based on the WRF model, we calculate the observation priors from the model outputs written to the disk. A flow chart of the 4DEnSRF procedure is given in Figure 1. Compared with the standard sequential EnSRF where observations are grouped into batches and analyzed at the analysis times, 4DEnSRF analyzes observations collected at different times of the assimilation window simultaneously, with observation priors calculated from the background forecast states at the observation times.

Unlike the cases of 4D-LEnKF (Hunt *et al.*, 2004) and 4D-LETKF (Hunt *et al.*, 2007), the WH02 EnSRF algorithm on which 4DEnSRF is based analyzes observations one after another. After an observation is analyzed, the new analysis becomes the background for the next observation, and typically the prior of the next observation is computed from this new background. In Eqs (17) and (18), only model states at the analysis time are updated, while at other times observation priors should be updated by the filter/smoothing. Thus it is necessary to write separate equations for updating these priors, including their ensemble mean and ensemble perturbations (the observation priors also can be considered part of an extended state vector).

For the j th observation, y_j^o , the update equations for the observation prior ensemble mean, \bar{y} , and deviations from the ensemble mean, \mathbf{Y}' , are, respectively:

$$\bar{y}^a = \bar{y}^b + \boldsymbol{\rho}^o \circ \mathbf{K}_j^o (y_j^o - \bar{y}_j^b) \quad (20)$$

$$\mathbf{Y}'^a = \mathbf{Y}'^b - \alpha \boldsymbol{\rho}^o \circ \mathbf{K}_j^o \mathbf{Y}'_j^b, \quad (21)$$

where \mathbf{K}_j^o is the Kalman gain for the j th observation, with its k th element equal to

$$K_{j,k}^o = \frac{\sum_{i=1}^m y_{ij}^b y_{i,k}^b}{\sum_{i=1}^m y_{ij}^b y_{ij}^b + R_j}. \quad (22)$$

In Eqs (20) and (21) symbol \circ in the equations represents the Schur (element-wise) product, $\boldsymbol{\rho}^o$ is the localization coefficient factor for the observation prior, which in our case

is expressed as $\boldsymbol{\rho}^o = (\boldsymbol{\rho}_t \boldsymbol{\rho}_s^o + \boldsymbol{\rho}_{\text{hf}})/2$, and the two terms on the right-hand side are the static and flow-dependent parts, respectively. $\boldsymbol{\rho}_s^o$ is a spatial localization factor that is specified as a function of the distance between the observation being processed and the observation prior being updated. $\boldsymbol{\rho}_t$ is a temporal localization factor that is a function of the time interval between the two observations. For the flow-dependent part, $\boldsymbol{\rho}_{\text{hf}}$, we adopt the hierarchical filter (HF) idea of Anderson (2007) with $\boldsymbol{\rho}_{\text{hf}}$ being the regression confidence factor (RCF) of the HF. Equal weight given to the static and flow-dependent parts was found to work well based on earlier tests. A combination of the static and flow-dependent parts to form a 'hybrid' localization scheme is beneficial because the flow-dependent part based on the HF is also subject to sampling error.

With the above algorithm, for a given observation y_j^o , priors for those observations within the time window that have not been analyzed are first updated using Eqs (20) and (21). State variables are then updated using Eqs (17) and (18).

Updating the observation priors using the filter is equivalent to updating the model state and then calculating the observation priors from the updated state when the observation operator is linear. Anderson and Collins (2007) proposed a variant of the serial EnKF that is more friendly to parallel processing. It precomputes observation priors in parallel and updates them like state variables rather than recalculating them from the updated state. Therefore, this variant is referred to as parallel EnKF (PEnKF). In the case that all data are synchronously observed at the analysis time, and when our 4DEnSRF also updates observation priors at the analysis time, the 4DEnSRF and PEnSRF become the same.

Using the most recently updated observation priors and the state ensemble and including the localization, the state update equations for j th observation are

$$\bar{\mathbf{x}}^a = \bar{\mathbf{x}}^b + \boldsymbol{\rho} \circ \hat{\mathbf{K}}_j (y_j^o - \bar{y}_j^a), \quad (23)$$

$$\mathbf{X}'^a = \mathbf{X}'^b - \alpha \boldsymbol{\rho} \circ \hat{\mathbf{K}}_j \mathbf{Y}'_j^a, \quad (24)$$

where the k th element of Kalman gain $\hat{\mathbf{K}}_j$ is

$$\hat{K}_{j,k} = \frac{\sum_{i=1}^N x'_{i,k} y'_{ij}^a}{\sum_{i=1}^N y'_{ij}^a y'_{ij}^a + R_j}. \quad (25)$$

Similarly, $\boldsymbol{\rho} = (\boldsymbol{\rho}_t \boldsymbol{\rho}_s + \boldsymbol{\rho}_{\text{hf}})/2$ in the equations is the localization factor for state variables for a given observation. The flow-dependent part has the ability to account for movement of features during the assimilation window. We should point out here that the use of temporal localization will break the formal equivalence between the four-dimensional asynchronous algorithm and the sequential synchronous algorithm that assimilates data at the observation times, even in the case of a perfect linear model and linear operator; the localization is, however, necessary to alleviate the negative impact of covariance sampling error, especially when the time window is long.

In summary, 4DEnSRF in a single analysis cycle involves three steps: (i) the calculation of all observation priors at the times observations are taken; (ii) the update of observation

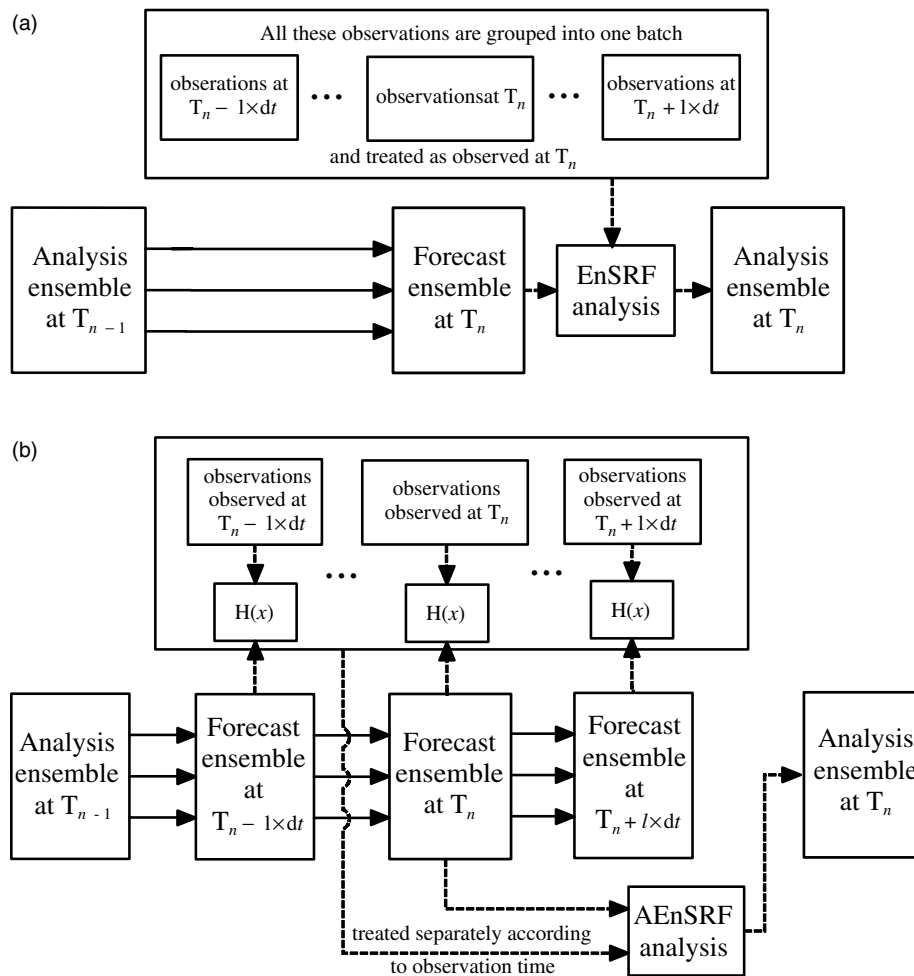


Figure 1. Flow charts of (a) regular synchronous EnSRF and (b) four-dimensional asynchronous EnSRF (4DEnSRF), where T represents the analysis time; dt denotes the time interval for processing observation priors and l indicates the number of times this process is conducted. The solid lines with arrow head indicate ensemble forecasts while the dashed lines indicate input/output processes.

priors; and (iii) the update of model states. Steps (ii) and (iii) are repeated for each observation serially until all observations in the current time window are processed.

3. OSSE experiments

3.1. Model configuration and truth simulation

The weather research and forecast (WRF) model V2.2.1 (Skamarock *et al.*, 2005) is used for the truth simulation and OSSEs. In the truth simulation, a fast-moving, splitting supercell storm is simulated, triggered by a thermal bubble in a horizontally homogeneous environment. This environment is defined by a classic Weisman and Klemp (1982) analytic sounding and is shown in Figure 2. The wind profile is made up of a quarter circle in the lowest 7 km and then a straight westerly hodograph above, plus a uniform (10, 10) m s^{-1} wind vector added to the entire wind profile. For all experiments, the domain is 120 km \times 120 km \times 20 km with $61 \times 61 \times 41$ grid points. The horizontal grid spacing is 2 km and the vertical grid spacing is 0.5 km. A 3 K ellipsoidal thermal bubble with a horizontal radius of 10 km and a vertical radius of 1.5 km is centred at $x = 10$ km, $y = 30$ km and $z = 1.5$ km. Other model parameters used include: Runge-Kutta third-order time-integration scheme with a time step of 12 s, WRF single-moment 6-class (WSM6) microphysics, and

the rapid radiative transfer model (RRTM) and Dudhia schemes for long- and short-wave radiation. No cumulus parametrization is included. A 1.5-order turbulent kinetic energy (TKE) closure scheme is used to parametrize subgrid-scale turbulence and a positive definite scheme is used for the advection of moisture and water variables. Open conditions are used at the lateral boundaries. More details with regard to these parametrization schemes can be found in Skamarock *et al.* (2005). The length of simulation is 95 min.

Three stages of the simulated storm are plotted in Figure 3. At 30 min, the storm is approximately centred at $x = 35$ km, $y = 45$ km, about 15 km northeast of its initial location. There are two updraft maxima in the storm, corresponding to the start of cell splitting. At 60 min, two separate cells and updraft cores are established and at 5 km above ground level (AGL) the updrafts of the right moving and left moving cells (hereafter RC and LC) reach about 30 m s^{-1} and 20 m s^{-1} , respectively. At 90 min, the two cells drift further apart and both remain rather strong. The maximum updraft of the RC reaches 45 m s^{-1} during the simulation and its cloud top reaches 15 km AGL.

3.2. Simulation of radar observations

In this study, observations are simulated for a radar located at $x = 0$ km, $y = 90$ km, and its maximum range is enough to cover the entire model domain. In the vertical, the

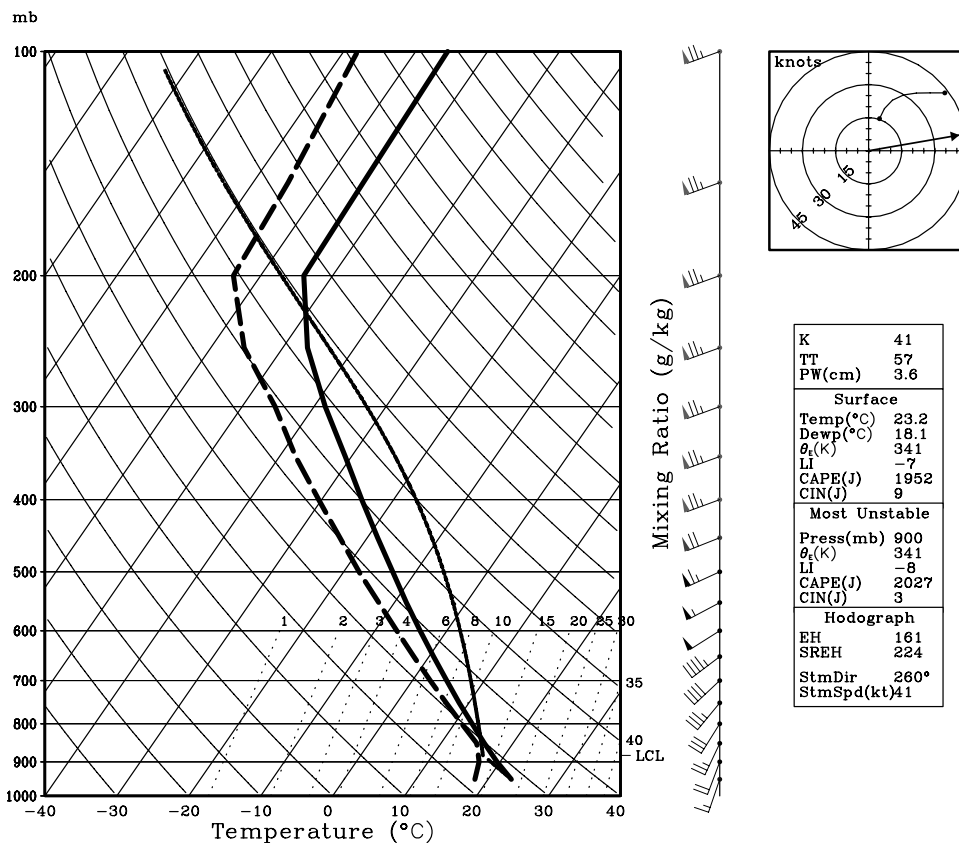


Figure 2. The environmental sounding for truth simulation, where the bold solid line represents the profile of temperature, bold dashed line represents the dewpoint temperature. The vector in the hodograph is the estimated storm motion vector.

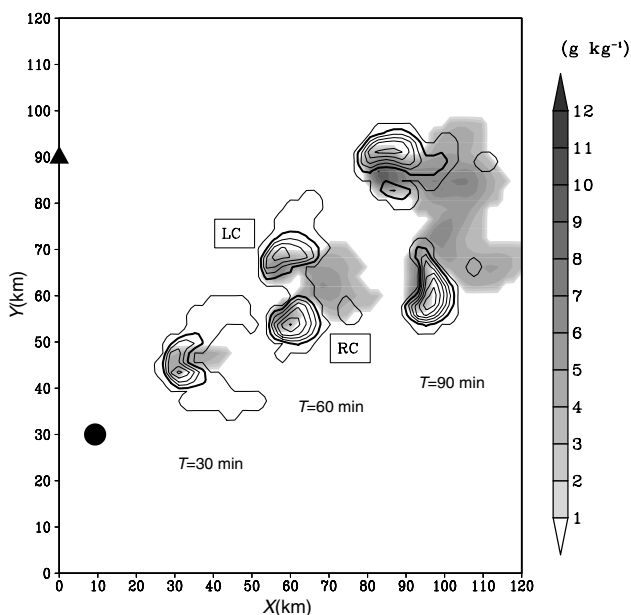


Figure 3. w (contour at 5 m s^{-1} interval) and q_g (shaded) at 5 km above ground level for truth simulation at 30 min (left), 60 min (middle) and 90 min (right). w with value of 5 m s^{-1} is plotted with the bold contour. The location of the initial thermal bubble is marked by a dot and that of the simulated radar is marked by a triangle.

observations are simulated on radar elevation levels, as in recent OSSE articles (e.g. Xue *et al.*, 2006; Lei *et al.*, 2007). In the horizontal direction, observations are assumed to be mapped to the model grid points already, a common practice with radar DA (e.g. Xue *et al.*, 2006). The radar

operates in the standard US WSR-88D volume scan pattern (VCP) 11, which has 14 elevation angles ranging from 0.5° to 19.5° . Each volume scan spans 5 min. Following Yussouf and Stensrud (2010), the lowest 12 elevations of observations are collected at a rate of three elevations per minute and the upper two elevations are collected during the last minute of each volume scan with observations stored in data files minute-by-minute. Data in each file are assumed to be observed simultaneously and these 1 min data files are referred to as raw data files. The first raw data file is at 21 min of model time.

Simulated observations are calculated using the observation operators, from model variables interpolated to the model scalar points in horizontal direction and radar elevations in the vertical direction. For radial velocity V_r , the observation operator is

$$V_r = u_g \cos \theta \sin \phi + v_g \cos \theta \cos \phi + (w_g - w_t) \sin \theta, \quad (26)$$

where u_g, v_g and w_g represent the model forecast wind components at radar observation points interpolated from the staggered model grid points, w_t represents the terminal fall speed of hydrometeors, and θ and ϕ represent the elevation angle and azimuth angle of the radar beam, respectively. For simulated reflectivity Z , the observation operator follows the formulae of Smith *et al.* (1975), which are also used in Tong and Xue (2005) and Xue *et al.* (2006),

$$Z = 10 \log_{10} \left(\frac{Z_r + Z_s + Z_h}{1 \text{ mm}^6 \text{ m}^{-3}} \right), \quad (27)$$

where Z_r, Z_s and Z_h are the equivalent reflectivity factors for rainwater, snow and hail, respectively. The reflectivity

observation operator in Eq. (27) has strong nonlinearity. Random errors drawn from Gaussian distributions with zero mean and standard deviations of 2 m s^{-1} and 2 dBZ are added to radial velocity and reflectivity, respectively. Data are assimilated only where reflectivity exceeds 10 dBZ , as in earlier OSSE studies (Tong and Xue, 2005).

3.3. Assimilation experiments

In our 4DEnSRF implementation, model variables updated include wind components u, v, w , geopotential height ϕ , potential temperature θ , and the mixing ratios of water vapour q_v , cloud water q_c , rainwater q_r , cloud ice q_i , snow q_s and graupel q_g . A first-guess state is defined by the environmental sounding used in truth simulation. Random perturbations are added to this initial background to create an initial 40-member ensemble. These random perturbations have a Gaussian distribution with zero mean and standard deviation of 3 K for θ and 0.5 g kg^{-1} for q_v . The wind field is not perturbed. The perturbations are smoothed by a recursive filter (e.g. Gao *et al.*, 2004) with a horizontal correlation scale of 2 km and a vertical correlation scale of two model levels, and are added at grid points only where reflectivity is $> 10 \text{ dBZ}$. The effect of this procedure is similar to that used in Tong and Xue (2008) and is computationally more efficient. The relaxation inflation scheme of Zhang *et al.* (2004) is used to help maintain the ensemble spread, according to

$$\mathbf{X}'_{\text{new}} = (1 - \gamma)\mathbf{X}'^a + \gamma\mathbf{X}'^b, \quad (28)$$

where \mathbf{X}'_{new} is the inflated posterior ensemble, and γ is the weight of the background ensemble, set to 0.5 as in Zhang *et al.* (2004). Additional inflation is further applied every 5 min by scaling the spread of θ to 2 K in the areas influenced by observational data in the filter updating. A fifth-order correlation function of Gaspari and Cohn (1999) is used to calculate the localization coefficients for static localization in both space and time (ρ_s or ρ_s^o and ρ_t). The cut off radii for spatial localization are 6 km in the horizontal and 2 km in the vertical. For temporal localization, settings are experiment-dependent and will be given later. In the calculation of RCF ρ_{hf} of the hierarchical filter, 40 ensemble members are divided into eight groups of five members each.

For the purpose of comparison, we design pairs of experiments using 4DEnSRF and EnSRF respectively. These experiments mostly differ in the data batch lengths (cycle intervals), which vary from 1 min to 20 min (Table 1). The first two letters in the experiment names indicate the analysis scheme used: SE, AE and PE represent, respectively, synchronous or regular EnSRF, asynchronous 4DEnSRF and the Anderson and Collins (2007) parallel EnSRF in which observation priors at the analysis time are also updated and used in the filter analysis. All non-PE experiments calculate the observation priors at the analysis time from the latest updated state. The ' nM ' indicates the cycle interval (data batch length) as ' n ' minutes. A data batch consists of data files with times centred on the analysis. For example, in SE1M and PE1M, 1 min data batches valid at the analysis time are used; the pair examines the effects of nonlinear radial velocity (because of the involvement of terminal velocity w_t) and reflectivity observation operators in PEnSRF versus regular EnSRF. As discussed in section 2c, when all data are observed

synchronously, PEnSRF is equivalent to 4DEnSRF, therefore AE1M would be the same as PE1M. In SE3M, raw data files 1 min before and after the analysis time are assumed to be valid at the analysis time, while in AE3M they are used at their valid times; and similarly for other experiments with longer batch lengths. Here, we choose to update the model state at the middle of the assimilation window to minimize the temporal sampling error. In a nonlinear system, the closer the observations are to the analysis time, the better the linear approximation is.

In addition, 'P' in the experiment name indicates that only partial data are used. The number following 'P' represents the time interval of data used. For instance, 'P10' means 10 min of data centred at the analysis time are used in each cycle. The 'S' at the end of SE5MS means that the data are actually synchronous, created from the truth simulation at the instance of analysis. This is the case in SE5MS only, which is designed to measure the impact of data timing error on the EnSRF analysis only. In all experiments, we perform the first analysis at 21 to 25 min (depending on the cycle length), run the analysis cycles until 85 to 88 min and launch a deterministic forecast from the ensemble mean analysis at about 45 min. No forecast is launched for SE5MS. In AE20M and SE20M, a 20 min data batch is not valid at 25 min so for the first cycle a 10 min data batch is used.

4. Results and discussions

To simplify the presentation, the square root of mean difference total energy (DTE) is used to evaluate the performance of the assimilation algorithm:

$$\text{DTE} = \frac{1}{2} \left[(\delta u)^2 + (\delta v)^2 + (\delta w)^2 + \frac{C_p}{T_r} (\delta \theta)^2 \right], \quad (29)$$

where δ denotes the difference of the ensemble mean from the truth, $C_p = 1004.7 \text{ J kg}^{-1} \text{ K}^{-1}$ is the specific heat of dry air at constant pressure, and $T_r = 270 \text{ K}$ is the reference temperature. We added vertical velocity w compared to the DTE used in Meng and Zhang (2007). Furthermore, to evaluate errors in the moisture and hydrometer fields, we define

$$\text{HydroDTE} = \frac{1}{2} [(\delta q_v)^2 + (\delta q_r)^2 + (\delta q_s)^2 + (\delta q_g)^2], \quad (30)$$

where q_v, q_r, q_s and q_g are the mixing ratios of water vapour, rainwater, snow and graupel, respectively. Similar to previous radar OSSE studies (e.g. Tong and Xue, 2005; Xue *et al.*, 2006), DTE and HydroDTE diagnostics are calculated only at grid points where the truth reflectivity exceeds 10 dBZ . Meanwhile, we refer the square root of mean DTE and HydroDTE as RM_DTE and RM_HydroDTE for convenience.

4.1. High frequency (1 and 3 min) assimilation experiments

We first look at the results using 1 min update cycles or data batches. The analysis RM_DTE and RM_HydroDTE obtained in PE1M are found to be very close to those of SE1M throughout the assimilation. The differences between final analysis errors in PE1M and SE1M are about 0.3 m s^{-1} and 0.08 g kg^{-1} for RM_DTE and RM_HydroDTE, respectively.

Table 1. List of experiments, where the SE, PE and AE represent sequential EnSRF, parallel EnSRF (PEnSRF) and asynchronous 4DEnSRF, respectively; nM in the experiment name denotes the cycle interval or the length of data batch as ' n ' minutes; the Pn indicates only ' n ' minutes of data centred at the analysis time are used and S at the end of SE5MS means that the data used are connected synchronously at the analysis time.

Experiment name	Analysis scheme	Analysis start time	Analysis end time	Data batches	Temporal correlation scale	Forecast start time
SE1M	EnSRF	21	88	1 min	N/A	49
PE1M	PEnSRF	21	88	1 min	6 min	49
SE3M	EnSRF	22	88	3 min	N/A	49
AE3M	4DEnSRF	22	88	3 min	6 min	49
SE5M	EnSRF	23	88	5 min	N/A	48
SE5MS	EnSRF	23	88	5 min	N/A	N/A
AE5M	4DEnSRF	23	88	5 min	6 min	48
SE10M	EnSRF	25	85	10 min	N/A	45
AE10M	4DEnSRF	25	85	10 min	6 min	45
SE10MP5	EnSRF	25	85	5 min	N/A	45
AE10MP5	4DEnSRF	25	85	5 min	6 min	45
SE20M	EnSRF	25	85	1st cycle 10 min, others 20 min	N/A	45
AE20M	4DEnSRF	25	85	1st cycle 10 min, others 20 min	12 min	45
SE20MP10	EnSRF	25	85	10 min	N/A	45
AE20MP10	4DEnSRF	25	85	10 min	6 min	45
SE20MP5	EnSRF	25	85	5 min	N/A	45
AE20MP5	4DEnSRF	25	85	5 min	6 min	45

Therefore, only the RM_DTE and RM_HydroDTE for SE1M are plotted in Figure 4. Also, the forecast from PEnSRF analysis is similar to that from EnSRF analysis. In Figure 5, it can be seen that the locations of forecast updraft cores in PE1M and SE1M are very close to the truth for both LC and RC, with the position errors being less than 2 km in both experiments. The updraft maxima in both experiments reach 30 m s^{-1} and 20 m s^{-1} for RC and LC respectively, capturing the updraft strength well. These results suggest that the way updated observation priors are obtained (the only difference between the two experiments) does not affect the results much in our case even though nonlinearity exists with the reflectivity and radial velocity operators.

Next, we compare the results between slightly longer 3 min cycle length experiments. It can be seen in Figure 4 that the analysis RM_DTE and RM_HydroDTE for SE3M and AE3M are mostly similar to each other; however, there are two clear differences. One is that the RM_HydroDTE is reduced more slowly in AE3M than that in SE3M before 30 min. This probably is caused by the highly nonlinear model, because Eqs (13) and (14) are strictly valid only when the model is linear. Poor quality temporal covariance used in AE3M during the earlier cycles can be another reason. Another difference is that the analysis error in AE3M becomes smaller than that in SE3M in later cycles. In Figure 6 it can be seen that the 4DEnSRF analysis at 88 min matches the truth well at all levels, while the EnSRF analysis is not as good, especially within the dashed rectangle. In this area, the EnSRF analyzed fields lag behind (displaced to the west of) the truth fields. The radar beams plotted in Figure 6 indicate that the analysis in this area is produced using data observed at 87 min, which is 1 min earlier than the analysis time. Due to this timing error, spatial displacement error results in the EnSRF analysis for this moving storm (the storm movement speed is about 21 m s^{-1} in this period). When a deterministic forecast is launched from the analysis, the forecast error in AE3M is clearly smaller than that in SE3M. In Figure 5, even though the forecast storms in AE3M and SE3M look qualitatively similar, the w errors (red contours) are larger in SE3M (Figure 5(e)). In the RC region, w error exceeds 20 m s^{-1} in SE3M while that in AE3M is less than

10 m s^{-1} . The location errors with the updraft cores are also smaller with AE3M. These results indicate that even for a short 3 min cycle length, the asynchronous formation still improves the storm analysis and forecast.

We now go back to experiment SE1M to see if the short 1 min cycle length is beneficial. Figure 4 shows that the minimum analysis errors are reached at around 55 min in all three experiments; after that time, the errors remain level or increase somewhat, especially in SE1M. The analysis RM_DTE in SE1M increases to 3.2 m s^{-1} at 88 min compared with 2.1 m s^{-1} at 55 min, and among the three experiments the errors of SE1M are actually the largest at the end of the assimilation window. We believe this is at least partially caused by the analysis of incomplete volumes of data, two to three elevations at a time, when using 1 min cycles. Doing so has a tendency to introduce spatial discontinuity and hence imbalance in the model state. Evidence can be seen in Figure 7(a) that the error at the upper levels is large (over 10 m s^{-1}), accompanied by wave-like fluctuations having periods of 3–5 min, roughly matching the intervals at which radar observations at these levels are introduced into the system. The problem is more significant at the upper levels because the vertical resolution of observations is lower, and as a result the high-frequency gravity wave oscillations in the stratosphere are more difficult to analyze accurately from radar data. Another reason for the increased error level is the frequent stopping and restarting of the WRF model. Even without the assimilation of any data, a restart of a WRF run using its 'cold start' input file does not exactly reproduce the forecast of an otherwise non-stop run. It is because the WRF stores some state variables and diagnoses others, causing (small) differences in the model state after restart (such small differences are generally inevitable with typical weather models unless restart files with a full state dump are used). Figure 7(b) shows that the forecast error grows in time with a signature of downward error propagation. These results indicate that there is additional benefit of doing four-dimensional asynchronous EnKF even when computational cost is not an issue.

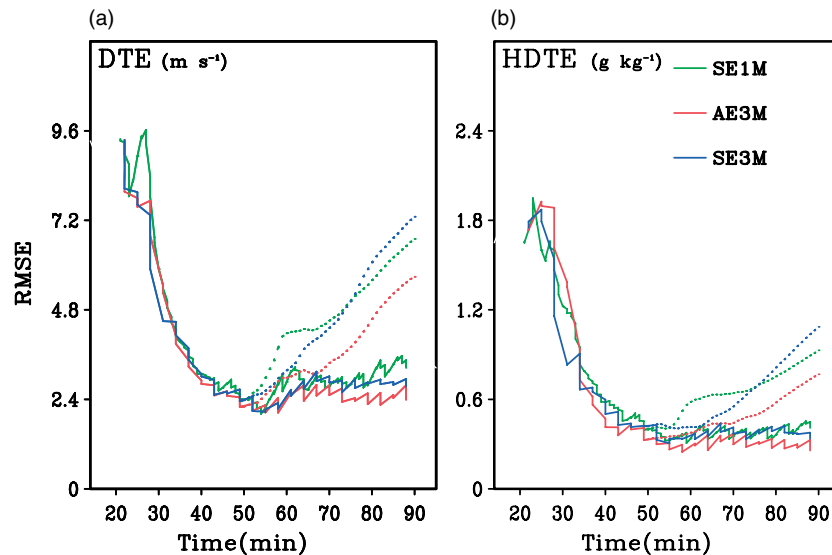


Figure 4. The (a) RM_DTE and (b) RM_HydroDTE for experiments SE1M, AE3M and SE3M. Solid lines represent the analyses and dashed lines represent the forecasts launched from the analysis ensemble mean at 49 min.

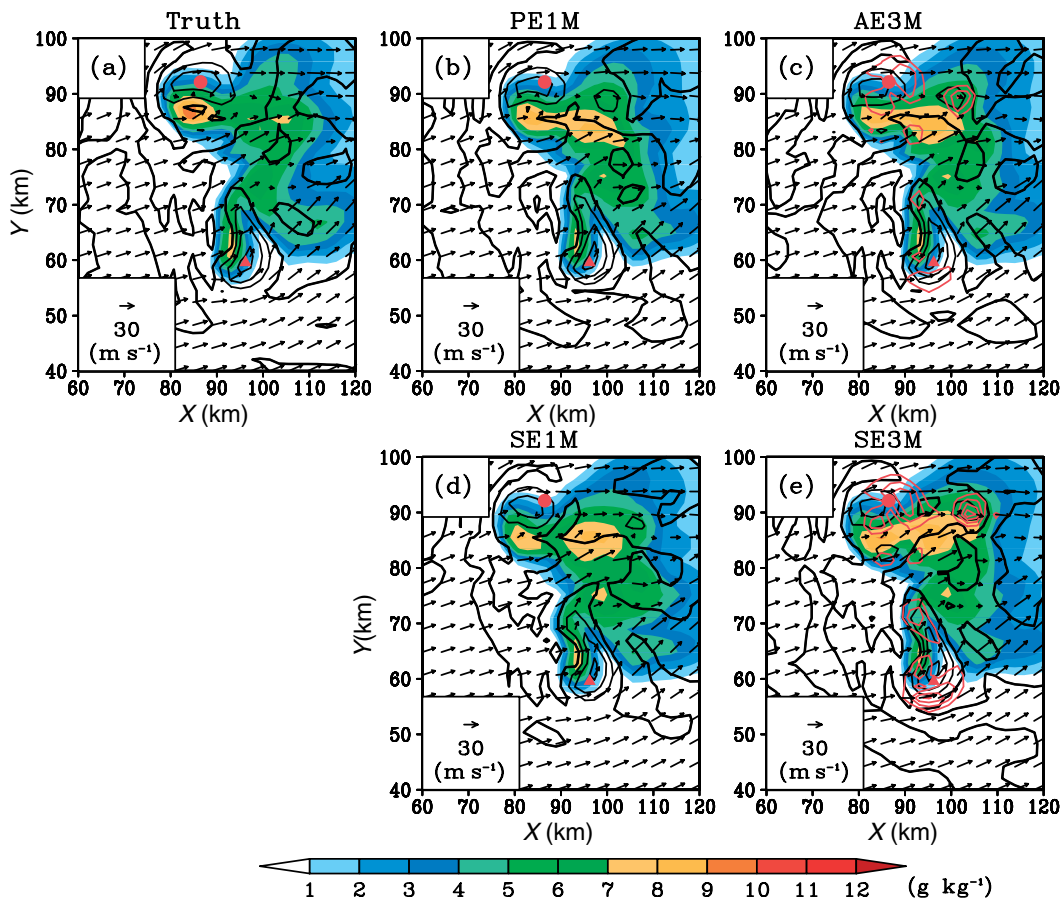


Figure 5. Horizontal wind (vector), w (black contours at intervals of 10 m s^{-1} , with the zero w contours also plotted) and q_g (shaded) at 5 km above ground level for (a) truth simulation and forecasts from (b) PE1M, (c) AE3M, (d) SE1M and (e) SE3M at 90 min, where the red triangle (dot) marks the location of updraft maximum of right (left) moving storm in truth simulation. The red contours (at intervals of 5 m s^{-1}) in (c) and (e) are for the absolute w forecast errors.

4.2. Assimilation experiments with longer cycle lengths

In this section we compare the performance of 4DEnSRF and EnSRF with longer cycle lengths. We first compare SE5M and AE5M, for which RM_DTE and RM_HydroDTE are plotted in Figure 8. From Figure 8(a) and (b) we can see that 4DEnSRF performs worse than EnSRF in

the early cycles but become much better later on (after 50 min or six cycles). At the end of assimilation, the analysis errors in AE5M are only half as large as those in SE5M for both RM_DTE and RM_HydroDTE. Similar behaviours were also observed earlier with SE3M and AE3M. Poor quality temporal covariance and model nonlinearity are suspected to be the causes. In other words, during

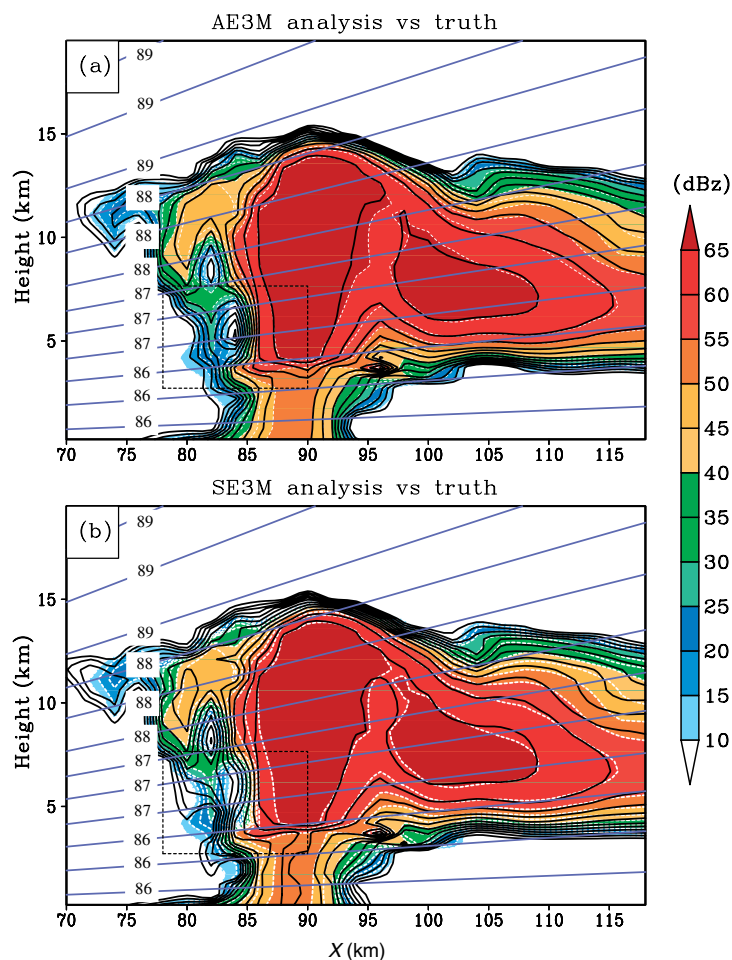


Figure 6. Vertical cross-sections of reflectivity at $Y = 58$ km for truth simulation (colour shaded and white dashed contours) and analyses (black solid contours) for (a) AE3M and (b) SE3M at 88 min. The purple straight lines represent the radar beam centres. The labels on the beams denote their observation times.

the earlier cycles when the state estimation and associated covariance is poor, data timing error in the regular EnSRF is secondary. Fortunately, as the state estimation improves, the asynchronous 4DEnSRF becomes superior (Figure 8(a) and (b)).

The time evolution of error profiles during the analysis and forecast periods are plotted in Figure 9 for AE5M and SE5M. We can see that analysis errors at the lower levels begin to increase after 60 min in SE5M (Figure 9(a)). Such errors are similar to the spatial displacement errors obtained earlier in SE3M, only larger in magnitude with the 5 min data batches (Figure 10). At this time in SE5M (Figure 10(a)), the analysis clearly lags behind the truth at the lower levels where data measured 2 min earlier are used (Figure 10(b)). The analysis in AE5M fits the observations almost perfectly (Figure 10(c)); correspondingly, the low-level errors in AE5M are much smaller late into the analysis period (Figure 9(b)). For forecasts launched from the analyses at 45 min, the error growth is also much slower in AE5M than SE5M, leading to the forecast errors at 90 min being substantially smaller in AE5M than SE5M (Figures 8(a) and (b) and 9(c) and (d)).

To demonstrate further that the larger error in SE5M came primarily from data timing error, experiment SE5MS is performed, which is identical to SE5M except that all simulated data were created (collected) at the exact times of analysis, 5 min apart. Therefore there is no timing error with the data. Figure 8(a) and Figure 8(b) show that the errors

of SE5MS are very close to those of AE5M, supporting our belief.

In addition, comparing Figure 9(b) with Figure 7(a) for AE5M and SE1M, respectively, clear differences are found at the upper levels. In AE5M, upper level errors gradually decrease as more data are assimilated while those in SE1M actually grow, again indicating the benefit of the asynchronous algorithm.

To further evaluate the performance of 4DEnSRF with longer cycle intervals, we examine the results from experiments having 10 or 20 min cycle lengths. In these cases, more than one radar full volume scan is available; they are either completely or partially used (Table 1). The analysis and forecast errors for these cases are shown in Figure 8(c)–(f). For these longer cycle lengths, the differences between 4DEnSRF and EnSRF algorithms are even larger. For a 10 min cycle length, the analysis errors in AE10M are below those of SE10M starting from just the second analysis cycle (Figure 8(c) and (d)), suggesting that the timing error in SE10M dominates possible poor state estimation even during early cycles (unlike the shorter cycle cases). At 45 min, the analysis RM_DTE in AE10M and AE10MP5 are reduced to about 2.4 m s^{-1} , as small as those in AE5M, and it remains at a similar level throughout the assimilation window. For RM_HydroDTE, the error level actually decreases further with cycles. Conversely, in SE10M and SE10MP5, the error levels are much higher; asymptotic levels of RM_DTE and RM_HydroDTE in SE10M and SE10MP5, at the end of

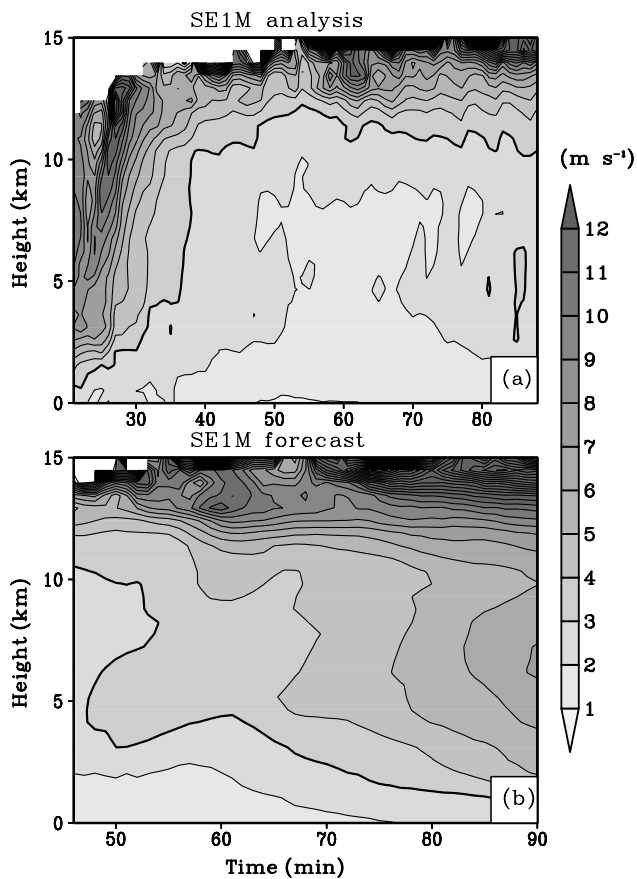


Figure 7. Time–height plots of RM.DTE for SE1M (a) analyses and (b) forecasts, where the bold contour represents the RM.DTE with value of 3 m s^{-1} .

assimilation cycles, are about 4.8 m s^{-1} and 0.6 g kg^{-1} , roughly twice those of AE10M and AE10MP5 (Figure 8(c) and (d)). It is also worth noting that the analysis errors of AE10M and AE10MP5 are similar, with those of AE10M being slightly lower, suggesting that when the asynchronous algorithm is used, the inclusion of observations beyond one volume scan interval can help the analysis (it at least does not harm). On the other hand, the errors at the end of the assimilation cycles are higher in SE10M compared with SE10MP5, indicating that the inclusion of additional data with larger timing error can actually harm the analysis.

Due to the smaller analysis errors, the errors of forecasts launched at 45 min are also smaller in AE10M and AE10MP5 than those in SE10M and SE10MP5 throughout the forecast period (Figure 8(c) and (d)). This advantage of the four-dimensional asynchronous algorithm becomes even larger when the cycle length is extended to 20 min. Figures 8(e) and 8(f) show that among all experiments with a 20 min cycle length, AE20M produces the lowest analysis and forecast errors while SE20M has the highest error levels. The differences in error are due, once again, to the large data timing errors that can occur in a 20 min cycle window. For such long cycle lengths, discarding data with large timing errors aids the regular EnSRF, as errors of SE20MP10 are lower than those of SE20M and errors of SE20MP5 are even lower. Note that the differences between SE20M and SE20MP10 are larger than those between SE20MP10 and SE20MP5 (Figure 8(e) and (f)). The errors of SE20MP5 are still higher than those of each asynchronous experiment. It is worth noting further that the analysis errors in AE20M

during the later cycles are not much higher than those of AE10M or even AE5M, which is important due to the associated computational savings using longer intervals.

Forecasts of the wind components and graupel mixing ratio at 90 min are plotted in Figure 11, together with absolute w forecast errors (in red contours). At this time, the forecast storm in AE5M looks very similar to the truth in almost all aspects; no non-zero w error contour is found in Figure 11(b) because its magnitude is smaller than 10 m s^{-1} , the contour interval. In comparison, there are large errors in w forecast in SE5M, with the error maximum exceeding 30 m s^{-1} , mostly associated with the lagging spatial displacement error with RC. This is consistent with the large errors at the end of the forecast in Figure 8(a) and (b). As the cycle length increases, the differences between 4DEnSRF and EnSRF become more evident. The northern cell in the forecasts of AE10MP5 and AE20M matches the truth well, with the absolute w forecast error being less than 10 m s^{-1} . In contrast, the errors associated with LC are much larger in SE10MP5 and SE20M in both graupel and w forecast fields, with the absolute w forecast error exceeding 10 m s^{-1} and 20 m s^{-1} in them, respectively. The updraft of the northern cell is mostly missing in SE20M (Figure 11(g)). Similar differences also can be found with the southern cell, but are more significant. Overall, the forecast storm pattern is clearly the worst in SE20M. The comparisons again confirm the benefit of 4DEnSRF over the regular EnSRF when assimilating frequent radar data using a cycle length 5 min or longer.

5. Summary and conclusions

In this study, a four-dimensional ensemble square root filter algorithm (4DEnSRF) is proposed for assimilating high-frequency asynchronous observations, such as those from weather radars. Given the serial nature of EnSRF, the 4DEnSRF algorithm precalculates observation priors from ensemble model states at observation times and updates the observation priors at asynchronous observational times to their posteriors using the filter; these posteriors, or the most recently updated observation priors, are used to update model state variables at the analysis time. Such an algorithm has the benefit of being able to utilize more observations collected over time using fewer analysis cycles, thereby reducing computational costs and potentially also improving filter performance. In our current 4DEnSRF implementation, a hybrid approach that combines static spatiotemporal localization with adaptive localization based on the hierarchical ensemble filter idea of Anderson (2007) is employed; the latter is in principle able to take into account system movement when localizing spatial covariances involving a time shift.

We tested the 4DEnSRF using simulated data from a single Doppler radar for a supercell storm. The radar data are simulated elevation by elevation and are grouped into data batches with different time intervals and assimilated with analysis cycles of the same lengths. Parallel sets of experiments using 4DEnSRF and the regular EnSRF are performed to compare their performance. Data batch or cycle lengths between 1 and 20 min are examined. The EnSRF always assumes that all data used in a given cycle are valid at the same analysis time. When the cycle length is 10 or 20 min, some experiments use only data taken within a 5 or 10 min time window centred on the analysis time.

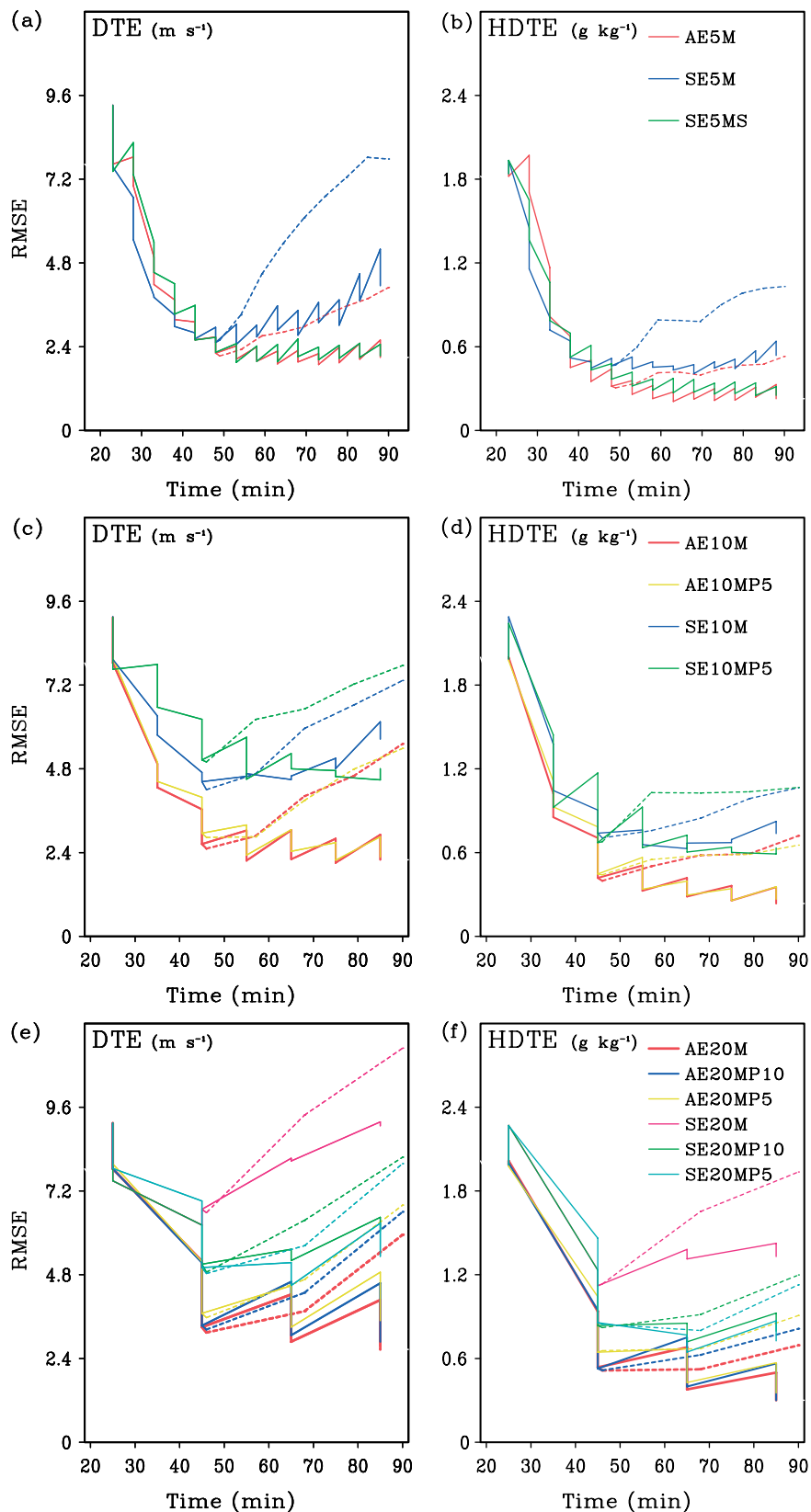


Figure 8. As in Figure 4, but for experiments with cycle lengths equal to or longer than 5 min. The experiments shown in each row are indicated in the legends in the right panels.

It is shown through OSSEs that 4DEnSRF performs better than EnSRF when the cycle length is 3 min or longer. Observation timing error is the main cause of the poorer performance of EnSRF for the analyses and for forecasts launched half way through the assimilation cycles; the longer

the cycle length, the larger the difference. For long cycle lengths, 4DEnSRF produces better analyses when utilizing all data at their correct times within the cycle window, but for EnSRF discarding data far away from the analysis time yields better analyses than using all data (those have timing

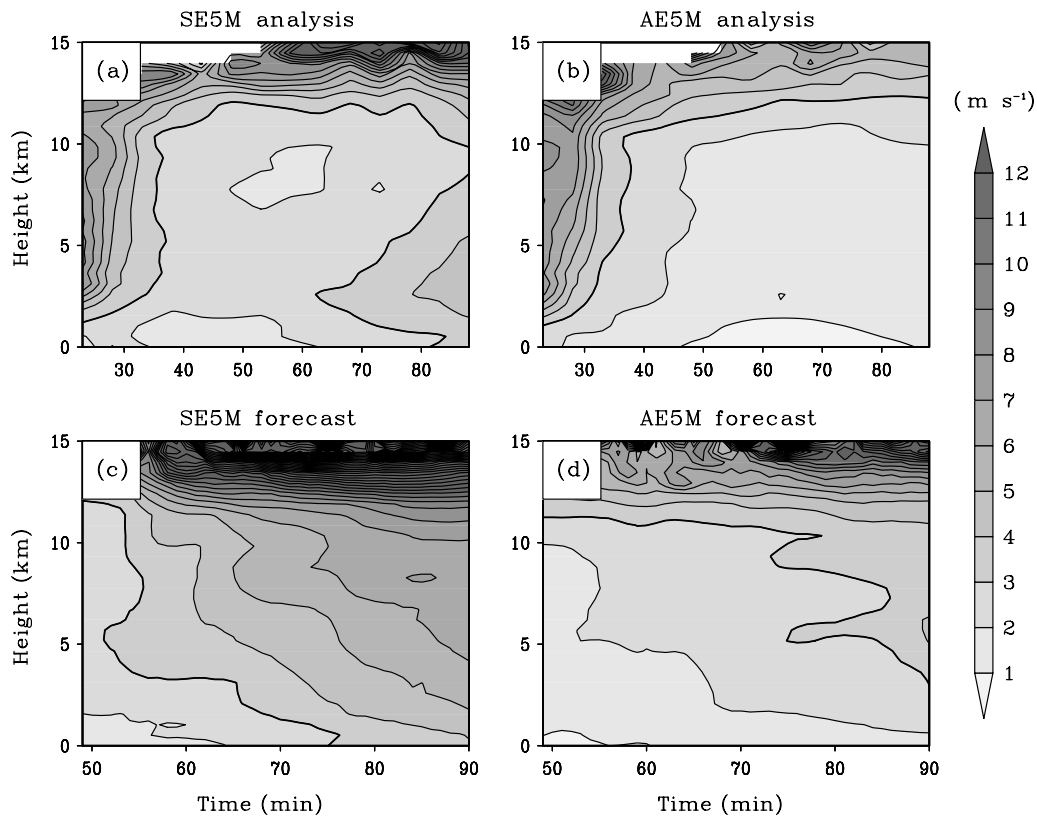


Figure 9. As in Figure 7, but for experiments (b, d) AE5M and (a, c) SE5M.

error). Assimilating only a couple of elevations at a time using very short (~ 1 min) cycles with regular EnSRF tends to introduce imbalances into the model state that degrades the subsequent analyses and forecasts.

More specifically, when the assimilation cycles are 3 min long, the 4DEnSRF analysis errors are smaller than those of EnSRF after the first few analysis cycles. The increase in error level in EnSRF was shown to be related mostly to the spatial displacement error of features that have moved between the times radar measurements were taken and the times at which such data are assimilated. This timing error in EnSRF comes from the assumption that all data were valid at the analysis time. The 4DEnSRF correctly uses the measurements at the times they were taken. The results with a 5 min cycle length were similar; although the differences between 4DEnSRF and EnSRF analyses and forecasts were somewhat larger.

When cycle interval is increased to 10 min or 20 min, the advantage of using 4DEnSRF becomes even more evident. In these cases, the impact of timing error dominates over other issues with the filters. With 4DEnSRF, the filter is able to reduce the analysis errors to levels close to those obtained using a 5 min cycle length even when a 20 min cycle length is used, while the error levels of the corresponding EnSRF analyses are about twice as large. The large error differences are also maintained in the forecasts launched from analyses midway through the analysis cycles.

Based on the OSSE results, several conclusions can be drawn: (i) the 'parallel' EnSRF algorithm that updates observation priors at the analysis time as part of the extended state vector performs comparably with regular EnSRF when tested with 1 min data batches/cycle length (hence data timing error is negligible); (ii) in the presence of data timing error with regular EnSRF, 4DEnSRF works better than

EnSRF; (iii) the advantage of 4DEnSRF becomes larger as the cycle increases, especially when the data span more than one radar volume scan interval; (iv) very short assimilation intervals (~ 1 min) can introduce shock and imbalance into the model state, which degrade the analysis and forecast; (v) when the assimilation cycle spans more than one volume scan, it is better for the regular EnSRF to use only the data from the closest scan volume in order to reduce the impact of timing errors in the data, while for 4DEnSRF using all data yields better results; (vi) overall, using 4DEnSRF with 5 to 10 min cycle lengths yields the best results for our test problem but the final analysis errors using a 20 min cycle length are only slightly larger. Considering the significant computational cost saving, the use of the four-dimensional algorithm with ~ 20 min cycles is attractive, especially for real-time applications. The 4DEnSRF algorithm also has been implemented in the full EnKF framework of the ARPS model with embedded (within the model) observation prior calculations. The system is being tested with real radar data and the results will be reported in a future article.

Acknowledgements

This work was supported primarily by NSF grant OCI-0905040, AGS-0802888, NOAA Warn-on-Forecast Project under NA080AR4320904, and grant KLME060203 from NUIST. Partial support was also provided by NSF AGS-0750790, AGS-0941491, AGS-1046171 and AGS-1046081. J. Min was also supported by the Meteorology Commonwealth Project of China (GYHY200806029) and the Cultivation Fund of the Key Scientific and Technical Innovation Project, Ministry of Education of China (No: 708051). Discussions with CAPS scientists, including Dr Youngsun Jung and Robin Tanamachi, had been beneficial. Computations were

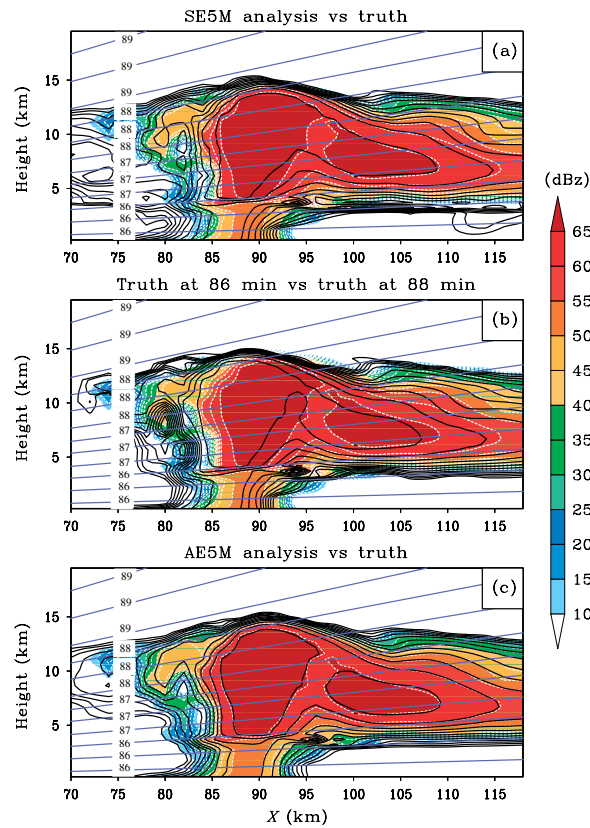


Figure 10. As in Figure 6, but for analyses from (a) SE5M at 88 min, (b) truth simulation at 86 min and (c) AE5M at 88 min. In (b), both shaded and solid contour represent the truth, where the solid contour represents the truth state at 86 min and the shaded represents the truth at 88 min.

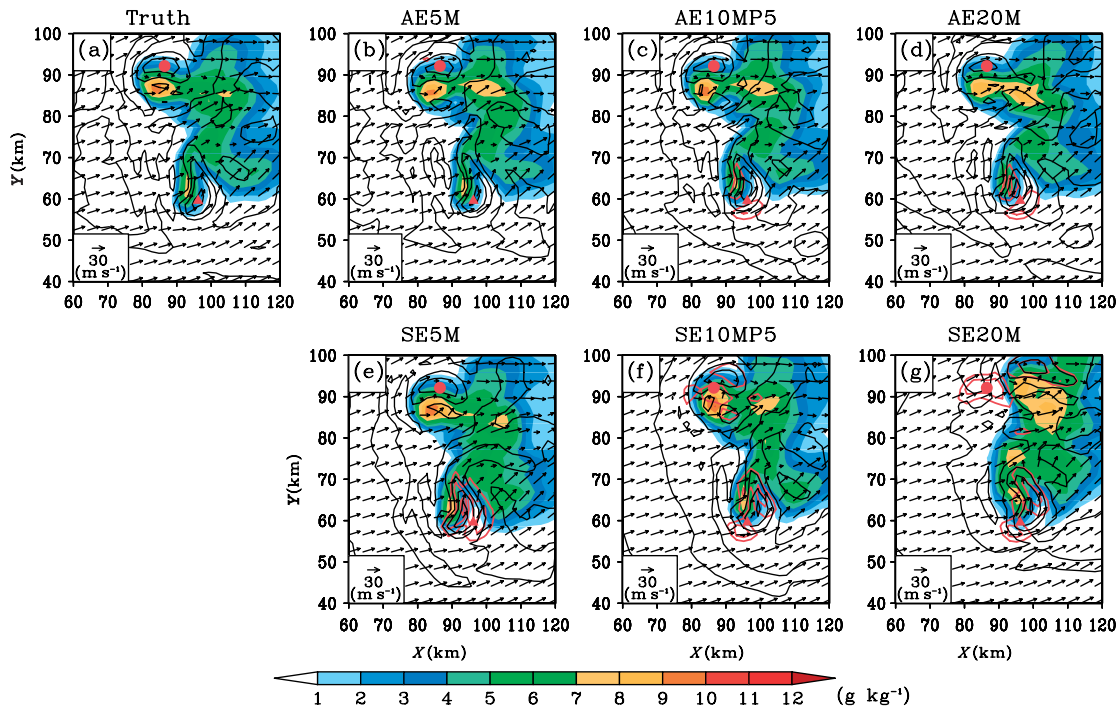


Figure 11. The same as Figure 5, but for experiments (b) AE5M, (c) AE10MP5, (d) AE20M, (e) SE5M, (f) SE10MP5 and (g) SE20M. The absolute w forecast errors are shown in red contours at intervals of 10 m s^{-1} .

carried out at the University of Oklahoma Supercomputer Center for Education and Research (OSCAR), and on the CAPS Linux Cluster machines. Nicholas Gasperoni is thanked for proofreading the manuscript. Comments by Dr Pavel Sakov and an anonymous reviewer improved the manuscript.

References

- Anderson JL. 2007. Exploring the need for localization in ensemble data assimilation using a hierarchical ensemble filter. *Physica D* **230**: 99–111.
- Anderson JL, Collins N. 2007. Scalable implementations of ensemble filter algorithms for data assimilation. *J. Atmos. Oceanic Technol.* **24**: 1452–1463.

- Compo GP, Whitaker JS, Sardeshmukh PD, Matsui N, Allan RJ, Yin X, Gleason BE, Vose RS, Rutledge G, Bessemoulin P, Bronnimann S, Brunet M, Crouthamel RI, Grant AN, Groisman PY, Jones PD, Kruk MC, Kruger AC, Marshall GJ, Maugeri M, Mok HY, Nordli O, Ross TF, Trigo RM, Wang XL, Woodruff SD, Worley SJ. 2011. The Twentieth Century Reanalysis Project. *Q. J. R. Meteorol. Soc.* **137**: 1–28.
- Dowell DC, Wicker LJ. 2009. Additive noise for storm-scale ensemble data assimilation. *J. Atmos. Oceanic Technol.* **26**: 911–927.
- Evensen G. 1994. Sequential data assimilation with a nonlinear quasi-geostrophic model using Monte Carlo methods to forecast error statistics. *J. Geophys. Res.* **99**: 10143–10162.
- Evensen G. 2003. The ensemble Kalman filter: Theoretical formulation and practical implementation. *Ocean Dynam.* **53**: 343–367.
- Evensen G, van Leeuwen PJ. 2000. An ensemble Kalman smoother for nonlinear dynamics. *Mon. Weather Rev.* **128**: 1852–1867.
- Gao JD, Xue M, Brewster K, Droegemeier KK. 2004. A three-dimensional variational data analysis method with recursive filter for Doppler radars. *J. Atmos. Ocean. Tech.* **21**: 457–469.
- Gaspari G, Cohn SE. 1999. Construction of correlation functions in two and three dimensions. *Q. J. R. Meteorol. Soc.* **125**: 723–757.
- Hu M, Xue M. 2007. Impact of configurations of rapid intermittent assimilation of WSR-88D radar data for the 8 May 2003 Oklahoma City tornadic thunderstorm case. *Mon. Weather Rev.* **135**: 507–525.
- Hunt BR, Kalnay E, Kostelich EJ, Ott E, Patil DJ, Sauer T, Szunyogh I, Yorke JA, Zimin AV. 2004. Four-dimensional ensemble Kalman filtering. *Tellus* **56**: 273–277.
- Hunt BR, Kostelich EJ, Szunyogh I. 2007. Efficient data assimilation for spatiotemporal chaos: A local ensemble transform Kalman filter. *Physica D* **230**: 112–126.
- Lei T, Xue M, Yu T, Teshiba M. 2007. Study on the optimal scanning strategies of phase-array radar through ensemble Kalman filter assimilation of simulated data. *33rd International Conference on Radar Meteorology*, Cairns, Australia. American Meteorological Society: Boston, MA; CDROM P7.1.
- Lorenz EN. 1996. Predictability: a problem partly solved. *Proceedings of the Seminar on Predictability*, European Centre for Medium-range Weather Forecasting, Reading; 40–58.
- Meng ZY, Zhang FQ. 2007. Tests of an ensemble Kalman filter for mesoscale and regional-scale data assimilation. Part II: Imperfect model experiments. *Mon. Weather Rev.* **135**: 1403–1423.
- Sakov P, Evensen G, Bertino L. 2010. Asynchronous data assimilation with the EnKF. *Tellus* **62**: 24–29.
- Skamarock WC, Klemp JB, Dudhia J, Gill D, Barker D, Wang W, Powers JG. 2005. *A Description of the Advanced Research WRF Version 2*. Technical Note NCAR/TN-468+STR, National Center for Atmospheric Research: Boulder, CO.
- Smith PL Jr, Myers CG, Orville HD. 1975. Radar reflectivity factor calculations in numerical cloud models using bulk parameterization of precipitation processes. *J. Appl. Meteorol.* **14**: 1156–1165.
- Snook N, Xue M, Jung J. 2011. Analysis of a tornadic mesoscale convective vortex based on ensemble Kalman filter assimilation of CASA X-band and WSR-88D radar data. *Mon. Weather Rev.* **139**: 3446–3468.
- Snyder C, Zhang F. 2003. Assimilation of simulated Doppler radar observations with an ensemble Kalman filter. *Mon. Weather Rev.* **131**: 1663–1677.
- Tong M, Xue M. 2008. Simultaneous estimation of microphysical parameters and atmospheric state with radar data and ensemble square-root Kalman filter. Part II: Parameter estimation experiments. *Mon. Weather Rev.* **136**: 1649–1668.
- Tong MJ, Xue M. 2005. Ensemble Kalman filter assimilation of Doppler radar data with a compressible nonhydrostatic model: OSS experiments. *Mon. Weather Rev.* **133**: 1789–1807.
- Weisman ML, Klemp JB. 1982. The dependence of numerically simulated convective storms on vertical wind shear and buoyancy. *Mon. Weather Rev.* **110**: 504–520.
- Whitaker JS, Hamill TM. 2002. Ensemble data assimilation without perturbed observations. *Mon. Weather Rev.* **130**: 1913–1924.
- Xue M, Wang DH, Gao JD, Brewster K, Droegemeier KK. 2003. The Advanced Regional Prediction System (ARPS), storm-scale numerical weather prediction and data assimilation. *Meteorol Atmos. Phys.* **82**: 139–170.
- Xue M, Tong M, Droegemeier KK. 2006. An OSSE framework based on the ensemble square-root Kalman filter for evaluating impact of data from radar networks on thunderstorm analysis and forecast. *J. Atmos. Ocean Tech.* **23**: 46–66.
- Yang SC, Kalnay E, Hunt B, Bowler NE. 2009. Weight interpolation for efficient data assimilation with the local ensemble transform Kalman filter. *Q. J. R. Meteorol. Soc.* **135**: 251–262.
- Yussouf N, Stensrud DJ. 2010. Impact of phased-array radar observations over a short assimilation period: observing system simulation experiments using an ensemble Kalman filter. *Mon. Weather Rev.* **138**: 517–538.
- Zhang F, Snyder C, Sun J. 2004. Impacts of initial estimate and observations on the convective-scale data assimilation with an ensemble Kalman filter. *Mon. Weather Rev.* **132**: 1238–1253.
- Zhang F, Weng Y, Sippel JA, Meng Z, Bishop CH. 2009. Cloud-resolving hurricane initialization and prediction through assimilation of Doppler radar observations with an ensemble Kalman filter. *Mon. Weather Rev.* **137**: 2105–2125.